43rd AIAA Plasmadynamics and Lasers Conference
25-28 Jun 2012, New Orleans, LS
AIAA-2012-2986

Aperture Effects on Aero-Optical Distortions Caused by Subsonic Boundary Layers

Adam E. Smith[1], Stanislav Gordeyev[2], and Eric Jumper[3]
University of Notre Dame, Notre Dame, Indiana, 46545

Results of experimental measurements of aero-optical distortions caused by turbulent boundary layers at subsonic speeds M = 0.4...0.6 are presented. Measurements were performed using a high-speed Shack-Hartmann sensor and a Malley probe to collect instantaneous wavefronts with high spatial and temporal resolution. Effects of different aperture sizes on levels of aero-optical aberrations and correlation lengths in both spanwise and streamwise directions are compared and discussed for both wavefront sensors. Detailed statistical analysis of spatial and temporal spectra of aero-optical distortions is presented. Analytical method to predict levels of aero-optical distortions and streamwise correlation lengths for different aperture sizes is proposed and it was found to agree with experimental results. The contribution of boundary-layer large- and small-scale structures on overall level of aero-optical distortions is examined and discussed.

I. Introduction

THE study of aero-optical effects is primarily focused on understanding and reducing the effect of turbulent aerodynamic flow fields on the propagation of optical wavefronts, in order to improve the performance of airborne optical systems [1,2]. The physical cause of aero-optical effects is a result of the relationship previously shown to exist between index of refraction and density through the Gladstone-Dale constant,

$$n(\boldsymbol{x},t) - 1 = K_{GD}\,\rho(\boldsymbol{x},t). \tag{1}$$

As a result of this relationship, perfectly-planar wavefronts propagating through three-dimensional, non-stationary density distributions present in turbulent aerodynamic flows are distorted. Given a refractive index field, the Optical Path Length (OPL) may be calculated by integrating the index-of-refraction, n, along the path of a ray; $OPL(\boldsymbol{x},t) = \int_{s1}^{s2} n(\boldsymbol{x},t)ds$. Optical Path Difference (OPD), which is the deviation from the mean path length , is defined by $OPD(\boldsymbol{x},t) = OPL(\boldsymbol{x},t) - \overline{OPL}(\boldsymbol{x},t)$, where the overbar denotes time averaging; OPD is typically the quantity of primary interest. It has been shown that OPD is the conjugate of the zero-mean wavefront such that $W(\boldsymbol{x},t) = -OPD(\boldsymbol{x},t)$ [3]. The aero-optical effects related to a number of aerodynamic problems including turbulent boundary layers, free shear layers, tip vortices, and flows around turrets have been studied in recent years [1,2]. Additionally, a number of experimental investigations have also analyzed the effectiveness of different flow control methods and adaptive-optic techniques for the mitigation of aero-optic effects [4,5].

While the study of the aero-optics of turbulent, compressible boundary layers has been ongoing for more than a half-century, [6] it is only in recent years that experimental wavefront sensing technology has achieved the temporal resolution required to study the significant features of aero-optically active flows [7]. The Malley Probe, described in detail by Gordeyev, et al. [8], makes high-bandwidth wavefront slope measurements at a discrete number of points in an aero-optically active flow, and then uses Taylor's Frozen-Flow hypothesis to reconstruct one-dimensional slices of wavefronts. A number of experiments have explored the relationship between aero-optical effects of turbulent boundary layers and a number of flow parameters including a Mach number, a boundary layer thickness, an angle of incidence, and wall temperature; scaling relationships were developed and shown to be consistent with experimental data [3,9-12]. Additionally, both experimental results [3,9-12] and recent computational results [6] have shown that the most optically-active structures within the subsonic turbulent

[1] Graduate Student, Department of Mechanical and Aerospace Engineering, Hessert Laboratory for Aerospace Research, Notre Dame, IN 46556, Student Member.
[2] Research Associate Professor, Department of Mechanical and Aerospace Engineering, Hessert Laboratory for Aerospace Research, Notre Dame, IN 46556, Senior AIAA Member.
[3] Professor, Department of Mechanical and Aerospace Engineering, Hessert Laboratory for Aerospace Research, Notre Dame, IN 46556, AIAA Fellow.

boundary layer convect at approximately 0.82 of the freestream velocity, which suggests that the most optically-active structures exist in the outer region of the turbulent boundary layer.

In addition to work using the Malley Probe to analyze the aero-optical effects of turbulent boundary layers, several authors including Cress [3] and Wittich, et al. [11] have also performed limited studies using low-bandwidth Shack-Hartmann wavefront sensors to measure the correlation lengths of optically aberrating structures within the turbulent boundary layer for different apertures, along with some estimation of the effect of aperture size on the level of optical aberrations observed. More recent turbulent boundary layer wavefront measurements performed by Wyckham & Smits [12] and Smith, et al. [13] have utilized high-speed digital cameras with frame rates on the order of tens of kHz's to capture boundary-layer-induced optical aberrations with good spatial and temporal resolution. High-bandwidth Shack-Hartmann wavefronts and 1-D Malley Probe wavefronts were compared in [13] and it was shown that there is good agreement between the two wavefront sensors when they are carefully compared.

From this ability to have good resolution in space and time for boundary layer wavefronts, more information about the physics of aero-optical aberrations can be obtained. In this paper, careful measurements of aero-optical distortions with high temporal and spatial resolution using both the high Speed Shack-Hartmann Sensor and the Malley probe were performed to calculate OPD as a function of space and time, for a number of different aperture sizes and freestream subsonic Mach numbers. The resulting correlation lengths, time-averaged and instantaneous wavefront statistics such as OPD_{rms}, as well as spectral statistics of the aero-optical aberrations acquired from each measurement method will be compared and discussed in detail. Contribution from different scales to the overall level of aero-optical aberrations will be estimated and discussed.

II. Experimental Setup

A. Facilities

Experimental measurements of the turbulent subsonic boundary layer were conducted at the Mach 0.6 closed-loop wind tunnel at the Hessert Laboratory for Aerospace Research - White Field at the University of Notre Dame, shown in Figure 1. The test section has a square cross section with sides of 91.4 cm and a length of approximately 2.75 m. Aero-optical measurements were collected through a turbulent boundary layer at stations located at 1.50m (at window #2) and 2.00 m (at window #3) from the start of the test section. We will herein refer to these two measurement locations as *W2* and *W3*, respectively. For all wavefront measurements at these locations, optical-quality glass windows were installed on opposite sides of the test section in order to provide clean optical access through boundary layers on both walls.

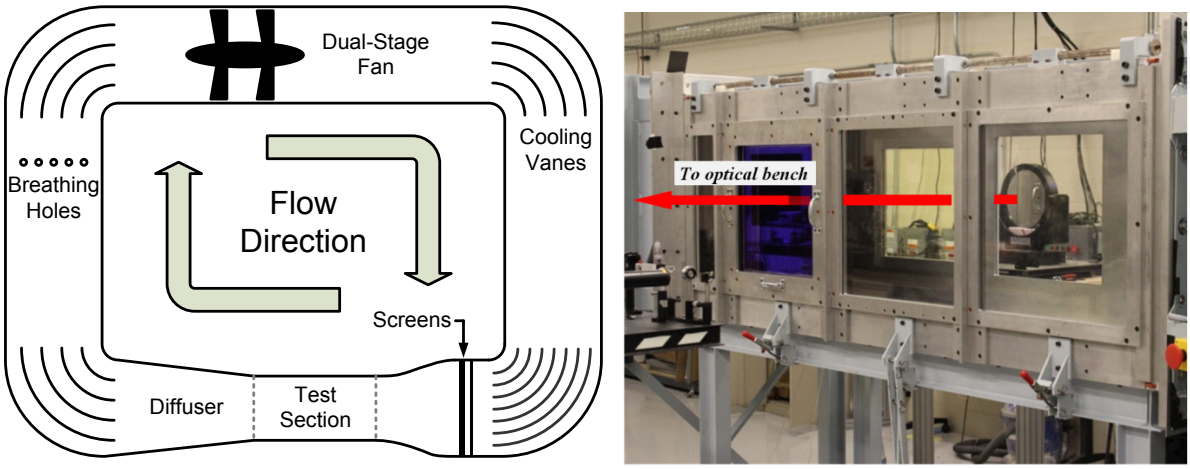

Figure 1. Schematic of White Field closed-loop wind tunnel (left), and a photo of the test section configured for boundary layer wavefront measurements (right).

The boundary layer at these measurement locations was previously characterized using a hot-wire anemometer to obtain mean velocity and velocity RMS profiles at freestream velocity M = 0.4. From these velocity surveys, boundary layer thicknesses at the beam center for both stations were shown to be approximately $\delta_{W2} = 3.2\ cm$ and $\delta_{W3} = 3.7\ cm$, with the momentum-thickness-based $Re_\theta \approx 7{\times}10^6$ [3]. During optical measurements, the freestream velocity was measured using a Pitot probe in the top wall, mounted upstream of the measurement location such that the probe wake would not interact with the wavefront-sensor beam path.

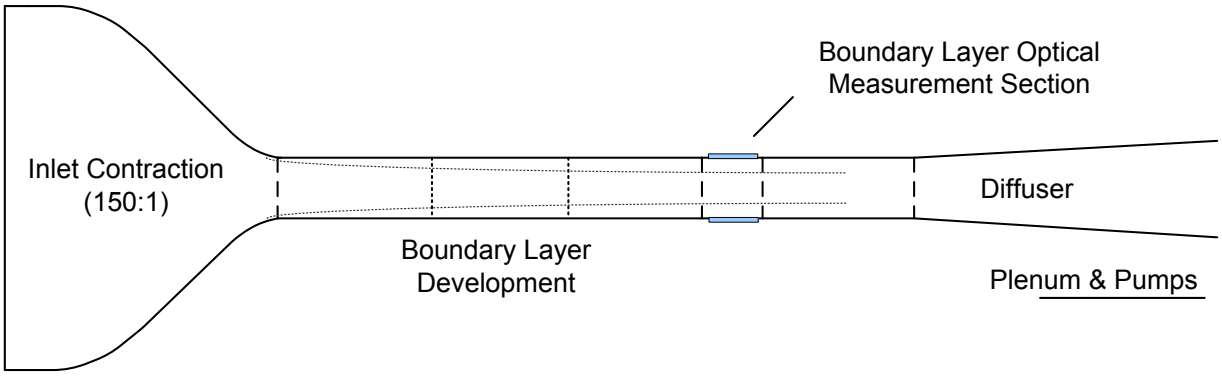

Figure 2: Schematic of the Hessert Laboratory transonic boundary layer wind tunnel.

Additional sets of measurements were taken in a transonic wind tunnel at the Hessert Laboratory for Aerospace Research at the University of Notre Dame. The wind tunnel, schematically shown in Figure 2, has an open circuit configuration with a 150:1 contraction ratio. With a cross section measuring 9.9 cm by 10.1 cm, the boundary layer test section has a development length of 155 cm from the contraction end to the optical measurement station. The freestream velocity was monitored using a Pitot-static probe. Previous Hot-wire characterizations of boundary layer development in this wind tunnel showed that the boundary layer thickness at the measurement section of the Hessert transonic wind tunnel, which we will denote as $H1$, was found to be $\delta_{H1} = 2.4\ cm$ [3].

B. Optical Wavefront Data Collection

Optical measurements were obtained using both the 1-D Malley Probe and High-Bandwidth Shack-Hartmann wavefront sensors. The test configurations for both wavefront sensors are shown in Figure 3. Assuming two statistically-independent boundary layers on opposite sides of the test section, combined wavefronts from both boundary layers were collected using both high-speed wavefront sensors, in order to achieve a higher signal-to-noise ratio. This method of measurement has been shown to agree well with single-pass boundary layer measurements once the proper correction is applied [3].

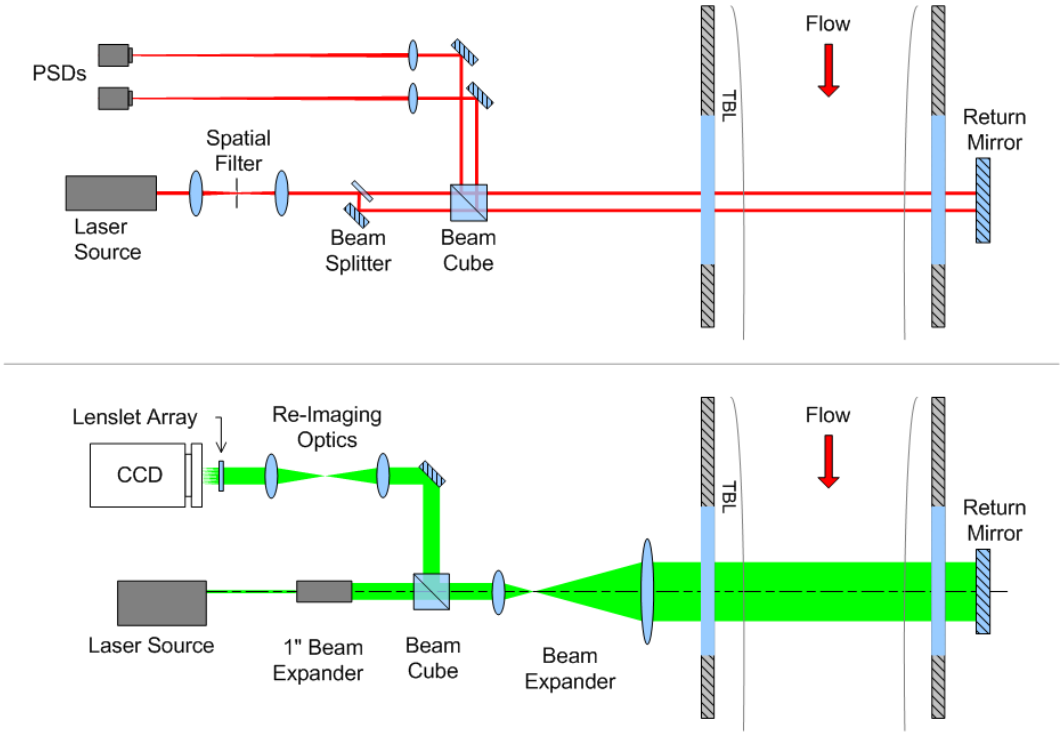

Figure 3. Schematic of optical set-ups for the Malley Probe wavefront sensor (top) and Shack-Hartmann sensor (bottom).

The Malley Probe 1-D wavefront sensor, the operating principles and data reduction methods of which are described in detail in [8], mainly replicates a single lenslet, or sub-aperture, of a Shack-Hartmann wavefront sensor using a small-diameter beam, $\sim O(1mm)$. From this beam, direct measurements of the beam deflection angle $\theta(t)$ can be made. Note that the deflection angle $\theta(t)$ is equivalent to the slope of the wavefront in the direction of mean flow, x, such that $\theta(x,z,t) = \frac{d}{dx}W(x,z,t) = -\frac{d}{dx}OPD(x,z,t)$. In the present study, deflection angle data were acquired for 10 seconds at 200 kHz. From the recorded deflection angle data, several quantities, including deflection angle amplitude spectra, one-dimensional wavefronts (A_{OPD}), and OPD_{rms} were computed via the frozen-flow assumption, $dx = U_c dt$, where the convective velocity U_c was found from the phase delay between simultaneous samples from two Malley Probe beams aligned in the mean flow direction which are separated by a some small separation Δ.

The spatially- and temporally-resolved 2-D boundary layer wavefronts were acquired using the high-speed Shack-Hartmann wavefront sensor described in [13], and shown in Figure 3 (bottom). Boundary layer wavefronts were collected at number of different sampling frequencies, spatial resolutions, and aperture diameters (Ap), which are shown in Table 1. These data were used to study the effects of aperture diameter, Ap on various statistical quantities including OPD_{rms}, wavefront spectra, and correlation lengths. Wavefront measurements were acquired at freestream Mach numbers between 0.4 and 0.6 for all experimental configurations noted in Table 1.

Facility	δ [cm]	Ap [in.]	f_{samp} [kHz]	Lenslet Resolution
White Field (*W3*)	3.7	1	9.5	60 × 60
"	"	2	9.5	60 × 60
"	"	4	9.5	60 × 60
"	"	4	25	30 × 30
White Field (*W2*)	3.2	10	10	30 × 30
Hessert Lab (*H1*)	2.4	2	49	30 × 15
"	"	4	49	30 × 15

Table 1: Two-Dimensional Wavefront acquisition parameters

C. Streamwise Variation of Boundary Layer Wavefronts

One of the potential problems in measuring spatially-resolved boundary layer wavefronts is that as streamwise aperture length increases, the effect of statistical variation in from boundary layer development becomes important to consider while analyzing two-dimensional wavefront boundary layer wavefront measurements. In [13], the authors have estimated the change in boundary layer thickness over some streamwise aperture length Ap via Prantl's $1/7^{th}$ power law for turbulent boundary layers;

$$\frac{\Delta\delta(Re_{Ap})}{\delta} = 0.23\frac{Re_{Ap}}{Re_{\delta}^{5/4}} + H.O.T. \tag{2}$$

If the first term in Eq. (2) is much less than one, then the variation in the boundary layer thickness over the aperture is considered to be negligible. For the cases reported in this study, the maximum measured streamwise aperture length was $Ap \cong 25$ cm $\cong 7..10\delta$, and the minimum Reynolds number was $Re_{\delta} = 2.2 \times 10^5$. Therefore, the maximum change in δ over the aperture is estimated to be approximately 11%. Based on this value, we can assume wavefront and boundary layer statistics are homogeneous in the streamwise direction over the length of the apertures in this study.

III. Aperture-Effects Correction of Wavefront Statistics

As shown in the previous section, for very large apertures Ap>>10δ, BL streamwise growth cannot be ignored and, for an infinitely-large aperture, aero-optical aberrations caused by boundary layers will be infinite. However, for most practical applications, aperture sizes are on the order of several boundary-layer thicknesses and, in this case, the boundary-layer can be assumed to be homogeneous in the streamwise direction and the frozen-field assumption can be used to trade the streamwise coordinate, x, and time, t, $x = -U_C t$.

Knowing the wavefront time-averaged spatial spectrum in the streamwise direction, $W(k_x) = \int_0^{\infty} W(x)\exp(-ik_x x)\,dk_x$, the level of aero-optical distortions, OPD_{rms}, and the streamwise correlation function, $R(\Delta x)$, for different apertures can be computed as,

$$OPD_{rms}^2 = 2\int_0^\infty G(k_x;Ap)\left|\widehat{W}(k_x)\right|^2 d(k_x/2\pi) \quad (3)$$

and

$$R(\Delta x) = 2\int_0^\infty G(k_x;Ap)\left|\widehat{W}(k_x)\right|^2 \exp(ik_x x)d(k_x/2\pi). \quad (4)$$

To account for the aperture effects, the wavefront spectrum should be modified by the inclusion of the wavefront aperture function, $G(k_x;Ap)$ [14], which works as a high-pass filter,

$$G\left(z=\frac{Ap\cdot k_x}{2\pi}\right) = \frac{-3-(\pi z)^2+(\pi z)^4+(3-2(\pi z)^2)\cos^2(\pi z)+6\pi z\sin(\pi z)\cos(\pi z)}{(\pi z)^4}, \quad (5)$$

As the local deflection angle is the spatial gradient of the wavefront, the streamwise wavefront spectrum can be calculated from the deflection-angle spectrum, using the frozen-field assumption, $k_x = 2\pi f/U_C$, as,

$$\widehat{W}(k_x) = U_C\hat{\theta}(f)/(2\pi f). \quad (6)$$

Thus, knowing the local deflection-angle temporal spectrum, we can compute OPD_{rms} and the streamwise correlation function for any aperture, less than 10 δ's, using Eqs. (3), (4) and (6).

IV. Experimental Results

A. Malley Probe Data Reduction

Time series of beam deflection angle data, $\theta(t)$, were acquired with the Malley Probe wavefront sensor, and the mean value of the deflection angle for each beam was removed. To remove the corrupting effects of significant low-frequency vibration imposed on beams during the experimental measurement, data were high-pass filtered at 500 Hz to reduce these effects. Deflection angle spectrum $\hat{\theta}(f)$ were computed for each Malley Probe beam, along with the spectral cross-correlation between beams, $S(f) = \langle\hat{\theta}_1(f)\,\hat{\theta}_2^*(f)\rangle$. Assuming that the wall is adiabatic, deflection angle spectra for a beam passing through the subsonic, turbulent boundary layer can be expressed in normalized form such that $\hat{\theta}_{NORM}(St_\delta) = \hat{\theta}(f)/\left(\frac{\rho}{\rho_{SL}}M^2\frac{\delta f_{SAMP}}{U_\infty}\right)$, where $f_{SAMP}$is the sampling frequency and $St_\delta = f\delta/U_\infty$ is the normalized frequency or Strouhal number. An example of the normalized deflection angle spectrum is shown in Figure 4, left plot.

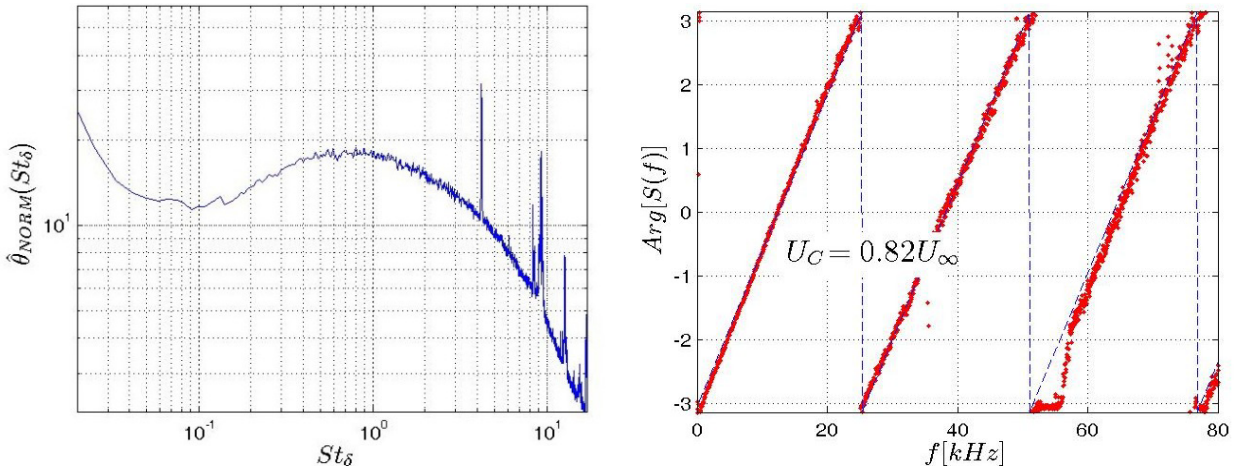

Figure 4: Normalized boundary layer deflection angle spectrum (left) and cross-correlation phase plot (right) obtained with Malley Probe wavefront sensor.

Consistent with previous results, the spectrum peak is observed near $St_\delta \sim 1$, which implies that prevailing aero-optically active structures are large, on the order of the boundary layer thickness δ. At reduced frequencies $St_\delta < 0.1$, an increase in amplitude spectrum is observed. The source of this increase is contamination from mechanical vibrations of optical components during testing, while the narrow-band peaks in the spectrum located near $St_\delta = 4, 9$ are a result of electronic noise. The spectral cross-correlation $S(f)$ is presented in Figure 4, right plot, and shows a linear relationship between phase over a wide band of frequencies. Recall that the phase slope is related to

the time delay τ, between the two beam deflection signals by $dArg[S(f)]/df = 2\pi\tau$. Therefore, average convective velocity can be computed as $U_c = \Delta/\tau$, where Δ is the beam separation distance. In this experiment, the streamwise convective velocity of aero-optically active boundary layer structures was found to be $0.82U_\infty$ for subsonic freestream velocities; this measurement is consistent with previous experiments discussed in the Introduction. In addition to these statistics, levels of wavefront distortions as a function of streamwise aperture, Ap, were computed after low-pass filtering deflection angle data by reconstructing a pseudo-spatial wavefront and dividing the time series into artificial apertures of different physical sizes, via the frozen flow approximation. Tip/tilt and piston were removed over each artificial aperture, and OPD_{rms} was computed over each aperture pseudospatial 1-D wavefront. For a detailed description of this method, the interested reader is referred to Cress, et al. [15].

B. Shack-Hartmann Wavefront Data Reduction

Wavefronts acquired with the high-bandwidth Shack-Hartmann sensor were calculated using commercially-available wavefront processing software. A detailed overview of the process for reducing these data is given by De Lucca, et al [16], to which the interested reader is referred for more information. The commercial software calculates wavefronts as a function of aperture coordinate and time. Time-averaged steady lensing and instantaneous tip/tilt and piston modes were removed from the data in post-processing. From these data, the spatial root-mean-square of OPD was computed at each instant in time in order to obtain the time series $OPD_{rms}(t)$; this quantity is directly related to the instantaneous Strehl ratio on a target. Examining the probability distributions of *OPD* and OPD_{rms} it was found that the data were in good agreement with previous Malley Probe results [15] indicating that their PDFs also have Gaussian and log-normal distributions, respectively.

A spectral analysis of spatially- and temporally-resolved wavefronts was also performed using the dispersion curve analysis discussed in detail by the authors in [13]. This calculation was performed by taking a 2-D 'slice' of wavefront data in x and t, $W(x, z = const, t)$, along the centerline of the aperture and computing its two-dimensional wavefront amplitude spectrum, $\widehat{W}(f, k_x)$. Normalizing this 2-D amplitude spectrum mapping in the following manner,

$$\widehat{W}_{NORM}(f, k_x) = \frac{\left|\widehat{W}(f, k_x)\right|}{\sqrt{\langle \widehat{W}(f, k_x)\rangle_{k_x} \langle \widehat{W}(f, k_x)\rangle_f}}, \tag{7}$$

we obtained a normalized wavefront-amplitude spectrum mapping which characterizes relative level of contribution to wavefront aberrations as a function of both a spatial and temporal frequency. By looking at the slope of the peak 'branches' in this normalized curve, convective velocity can be computed through the dispersion relation; $\omega(k_x) = k_x U_c(k_x)$.

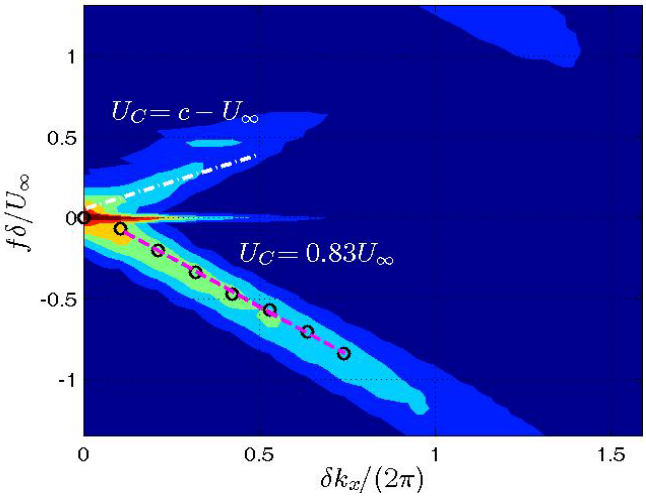

Figure 5: Spatial-temporal wavefront spectra and dispersion curves for a turbulent boundary layer

A typical normalized wavefront spectrum for boundary layer aero-optical measurements is shown in Figure 5, plotted as a function of normalized temporal and spatial frequencies. Note that there are three prominent 'branches' of peak values which start at zero and have linear slopes. The authors showed in [13] that the lower, or negatively sloped branch corresponds to aero-optical boundary layer aberrations, with contributions to aberrations coming from a wide range of spatial and temporal frequencies, and a convective velocity of $0.83U_\infty$. The horizontal, $f = 0$

branch, which corresponds to a convective velocity of 0, corresponds to a stationary optical feature. The upper branch was found to have a convective velocity of $c - U_\infty$, indicating that the source of these contributions to overall wavefront distortions come from acoustic disturbances propagating upstream from the tunnel driving fan through the diffuser section. To remove the non-boundary layer induced aberrations from further analysis, a 2-D spectral filtering method was used to remove aberrations which do not convect in the direction of freestream velocity.

C. One-Dimensional Wavefront Results

Recent careful comparisons between time-resolved 2-D wavefront measurements and 1-D Malley probe wavefront measurements have shown that there is significant low-frequency corruption in the Malley probe spectra from various sources [13]. It was shown in [13] that less-corrupted experimental measurements of the low-frequency (below-peak) deflection angle spectra can be obtained from time-resolved 2-D wavefront measurements, once correction for a finite-aperture size from [17] has been applied. This correction is necessary since wavefront tip/tilt removal has been shown to act as a high-pass filter function $\Gamma_{Ap}(\eta) = \left(1 - D_{Ap}^2\right)^{1/2}$, where $D_A = [3\sin(\pi\eta) - 3\pi\eta\cos(\pi\eta)]/(\pi\eta)^3$, and $\eta = 1.2(Ap/\delta)St_\delta$ [17]. A comparison of Malley-Probe spectra and aperture-corrected wavefront spectra is shown in Figure 6. The Malley Probe spectrum has vibration-related corruptions below $St_\delta < 0.5$ and a spectrum build-up at low frequencies below $St_\delta < 0.1$. Wavefront-based spectra also reveal the similar but smaller spectrum build-up at these low frequencies. Possible origins of these spectra build-ups are left-over mechanical vibrations and a slow drift in the freestream velocity of the tunnel. However, the exact behavior of the deflection-angle spectrum below $St_\delta < 0.1$.is not important, as it will be filtered out after applying the aperture transfer function (5).

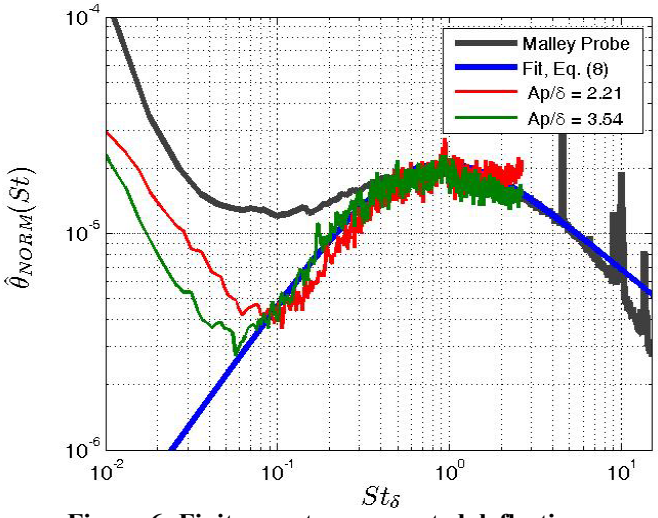

Figure 6: Finite aperture corrected deflection angle spectra compared with Equation 8.

Based on these observations, a new empirical fit is proposed for the streamwise deflection angle spectra:

$$\hat{\theta}_{OPD}^{fit}(St_\delta) = \hat{\theta}_{peak}\frac{St_\delta^m}{1 + \left(\frac{St_\delta}{St_{peak}}\right)^{\frac{2}{3}+m}} \tag{8}$$

where $\hat{\theta}_{peak}$ is the peak amplitude, St_{peak} is the peak location of the curve fit in Strouhal number space, and m is a real number which characterizes the behavior of the low-frequency end of the 1-D spectra, $\hat{\theta}(St_\delta) \sim (St_\delta)^m$. Equation 4, however, can be easily modified to explore other values of m, while preserving the well-established spectral behavior at high-frequencies. Based on finite-aperture-corrected spatially- and temporally-resolved wavefront measurement shown in Figure 6, the value of m it has been estimated from the low-frequency wavefront measurements to be m = 1.1.

As seen in Figure 6, the empirical fit does a good job of modeling the measured deflection-angle spectrum in the area of the peak location, as well as in the finite-aperture-corrected low-frequency end of the spectra, except the very low

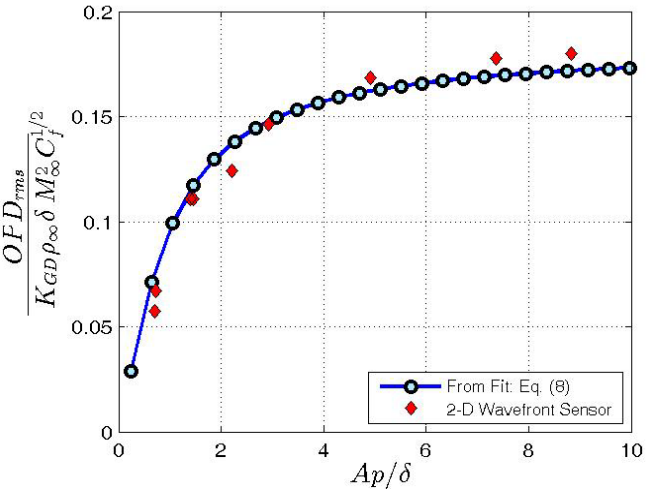

Figure 7: Comparison of predicted and measured OPD_{rms} for different aperture sizes.

frequencies $St_\delta < 0.1$. This very low end would affect wavefront statistics only for apertures larger than 10 δ's, where the presented spectra-based analysis would fail anyway due to streamwise evolution effects discussed in Section II.C.

Using the empirical fit, Eq. (8), and substituting it into Eqs. (3) and (5), the aperture effects on OPD_{rms} can be computed for a range of different apertures. Results are presented in Figure 7, along with experimental 2-D wavefront results, and show very good agreement. Note that high-pass filtering due to finite aperture diameter has a significant effect on OPD_{rms} for turbulent boundary layers.

D. Spatial Correlation Data

Streamwise and spanwise wavefront correlation data can be obtained from the 2-D wavefront data by computing autocorrelation maps for a large number of instantaneous wavefront realizations, and then averaging these instantaneous autocorrelation maps to calculate normalized time-averaged autocorrelation functions, $\rho(\Delta x, \Delta z) = R(\Delta x, \Delta z)/R(\Delta x = 0, \Delta z = 0)$ for a number of different aperture values. Examples of these data for two different aperture sizes are presented in Figure 8. Aperture effects primarily effect the streamwise correlation. Below we will discuss the streamwise and the spanwise correlation functions separately.

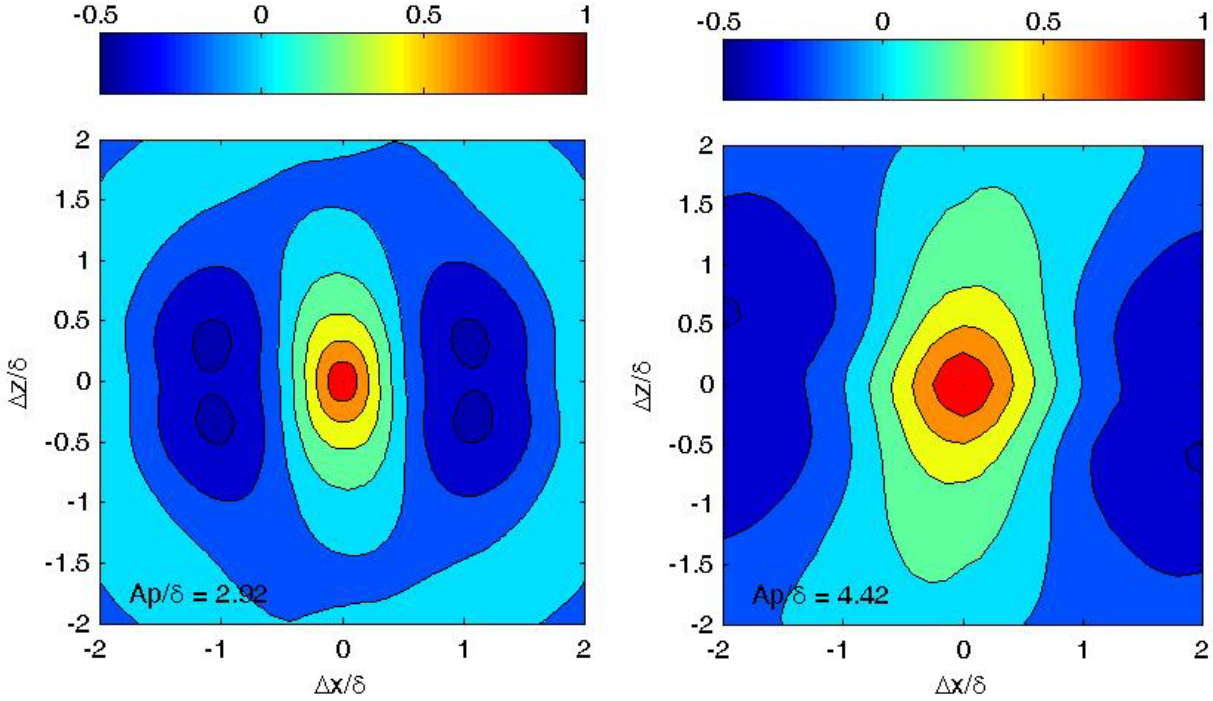

Figure 8: Time-averaged auto correlation maps for 2-D wavefront measurements.

1. Streamwise correlation

From experimental correlation function, streamwise correlation functions $\rho_x(\Delta x/\delta)$ were computed. The streamwise correlation function can also be computed from Eq. (4) and Eq. (6) using the empirical fit (8). The simulated correlation functions were calculated and the results of both experimental measurements and simulated correlation functions are presented in Figure 9, left plot. The experimentally-obtained and simulated correlation functions show good agreement up until approximately the first zero crossing. The reason of discrepancy between simulated and experimental results for large streamwise separations is most probably due to experimental error and, in lesser degree, the spectrum mismatch at very low end of the deflection-angle spectrum, observed in Figure 6. A comparison between streamwise correlation predictions from the present study and correlation functions obtained from CFD simulations by Wang and Wang [6] are shown in Figure 9, right plot. These data show good agreement up until approximately the first zero crossing as well.

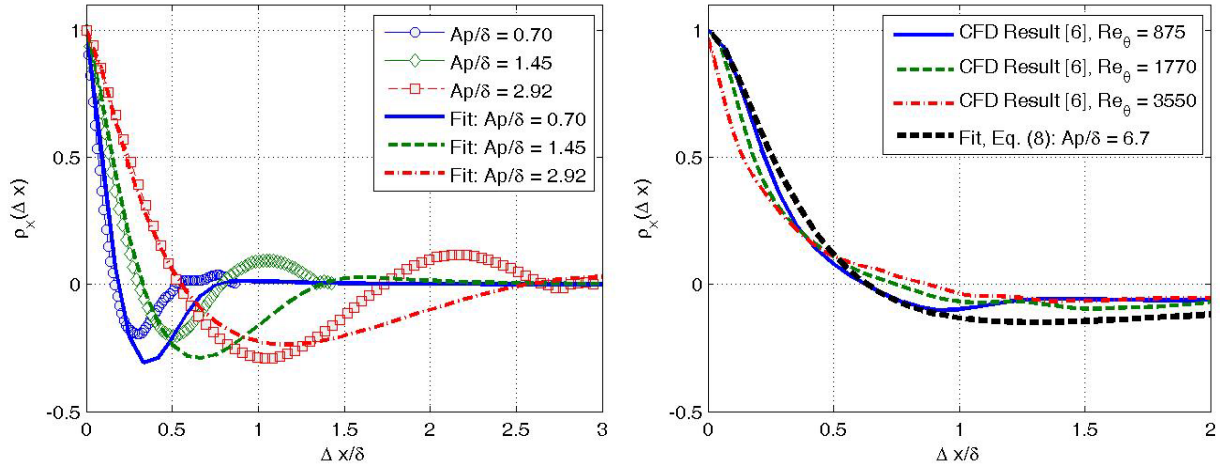

Figure 9: Streamwise wavefront correlation functions using analytical prediction (4) and experimental 2-D wavefront measurements (left) and comparison between the analytical prediction and CFD simulations [6] for $Ap/\delta = 6.70$ (right).

A comparison of all the results shows that the finite aperture size has a significant effect on the measured correlation function for boundary layer wavefronts. The effect of finite aperture size can be further characterized by computing the integral correlation lengths for each aperture correlation function. Correlation length Λ_x was computed by the equation

$$\Lambda_x\left(\frac{Ap}{\delta}\right) = \int_0^{\xi} \rho_x\left(\frac{\Delta x}{\delta}; Ap\right) d\left(\frac{\Delta x}{\delta}\right), \tag{9}$$

where ξ is the first value of Ap/δ which satisfies $\rho_x(\xi) = 0$ (i.e. the first zero-crossing point). Computed correlation lengths for both experimental and finite-aperture model predictions are presented in Figure 10. It was found that the length scale for both the experimental data and simulated correlation functions were in good agreement.

2. Spanwise correlation

Spanwise correlation functions $\rho_z(\Delta z/\delta)$ were also computed from the time-averaged correlation maps obtained from 2-D wavefront measurements, and the resulting functions are presented in Figure 11. It is observed that as we might expect from the streamwise correlation function results, the spanwise correlation function appears to be strongly dependent on aperture size. Malley probe and wavefront measurements from previous aero-optical studies from [3,11] and simulated wavefronts [6] are presented along with the 2-D wavefront data. While the 2-D wavefront data and 2-D computational data presented all appear to follow similar trends with regard to spanwise aperture size, Malley probe measurements do not match the 2-D wavefront data. This difference is likely due to the fact that while the Malley probe measurements were direct measurements of spanwise correlation, they are merely detecting average wavefront slope correlation in the spanwise direction. This discrete measurement method may be failing to capture some of the more complex dynamics of the system which are better resolved with the good spatial resolution available with the 2-D wavefront sensor.

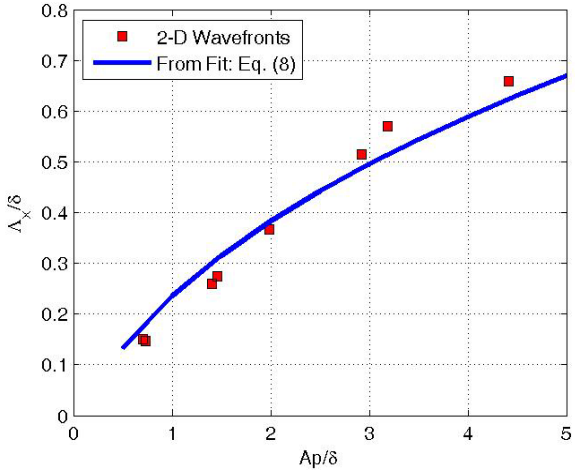

Figure 10: Streamwise correlation lengths.

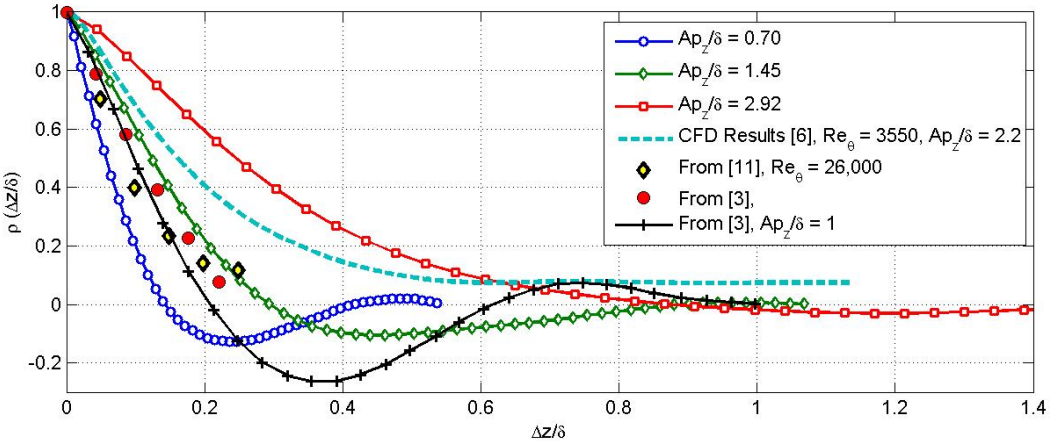

Figure 11: Spanwise correlation functions for different finite spanwise apertures Λ_z

E. Streamwise Correlation Length and OPD_{rms} scaling

All current statistical models for estimating levels of aero-optical distortion from turbulent boundary layers scale with by the local boundary-layer thickness; also both the level of optical aberrations and the streamwise correlation lengths were found to strong functions of the aperture size. Having now observed the effect of aperture size on wavefront levels and correlation lengths in the streamwise direction, we can check whether OPD_{rms} is linearly-proportional to the streamwise correlation length, Λ_x, as levels of atmosphere-related optical distortions do scale with the transverse correlation length. Figure 12 shows OPD_{rms} normalized by Λ_x for different aperture sizes; clearly this plot indicates that OPD_{rms}/Λ_x is still a function of the aperture size; thus the streamwise correlation length it is not an aperture-independent scaling length for boundary layer optical aberrations, proving again that aero-optical distortions have very different statistics compared to the atmospheric optical aberrations.

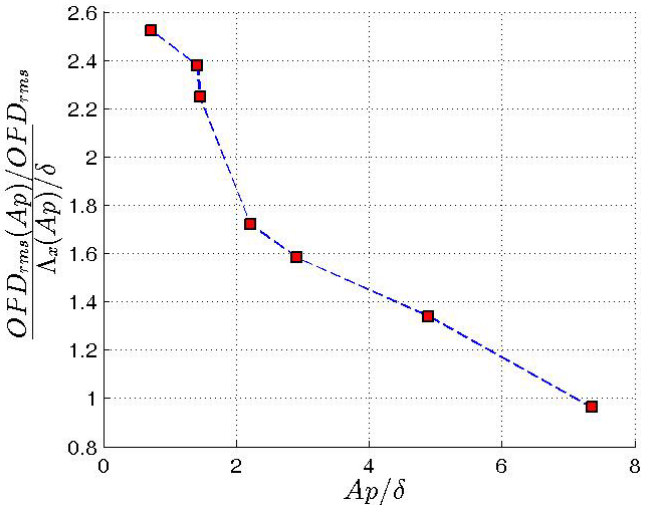

Figure 12: OPD_{rms} for different apertures normalized by the streamwise correlation length.

F. Effect of Large- and Small-Scale Structures

From Figure 7, which shows OPD_{rms} results both Malley Probe and 2-D wavefront measurements one can observe that levels of optical aberrations monotonically increase with the aperture size. Recalling that the tip/tilt removal on small-aperture 2-D wavefront measurements acts as a high-pass filter, another way of thinking about aperture effects is that the levels of optical aberrations measured for a certain aperture value correspond to the aberrations from structures with Strouhal number $St_\delta > St_{low} = 0.82(\delta/Ap)$. Figure 13 presents the levels of OPD_{rms} data from Figure 7, relative to the large-aperture limit shown from both sensors, re-plotted versus the low-

frequency cut-off Strouhal number, St_{low}. The experimental measurements indicate that boundary-layer structures corresponding to $St_{low} > 1$, which correspond to structures smaller than the boundary layer thickness, contribute only about 40% to the overall levels of optical distortions. As St_{low} increases above 1, the relative contribution of small scales continues to decrease even further, such that structures of sizes on the order of $\delta/2$ and smaller contribute only 20% to the overall level of optical aberrations.

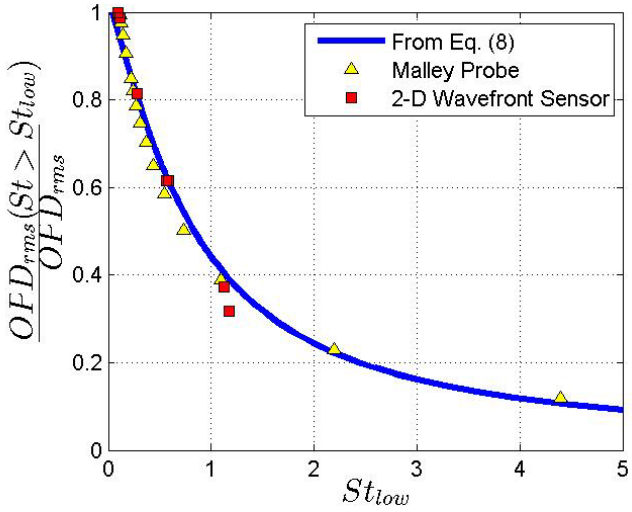

Figure 13: Contribution to OPD_{rms} from frequencies larger than St_{low}.

V. Conclusions

Experimental one- and two-dimensional wavefront measurements of subsonic, compressible turbulent boundary layers are presented for a number of different finite aperture sizes, and various corrupting effects were identified and discussed. The effect of finite aperture size on wavefront statistics and streamwise and spanwise correlation functions have been analyzed and discussed. An empirical curve fit for the spectral behavior of 1-D streamwise wavefront slices has been proposed. Used in combination with the finite aperture filter function, empirical-fit-predicted levels of aero-optical distortions agreed quite well with experimentally-observed results. Also, analytical predictions using the empirical fit for the streamwise correlation function demonstrated good agreement with 2-dimensional wavefront data and numerical simulations up until the first zero crossing. Thus, the analytical method using the proposed empirical fit for the deflection-angle spectrum was found to provide good prediction of OPD_{rms} and the streamwise correlation lengths for any apertures, which are less than approximately 10 boundary-layer thicknesses. For larger apertures, the frozen-field assumption, used in the modeling, is no longer valid, as the streamwise variation of the boundary layer has to be taken into account.

Spanwise correlation functions for wavefront measurements of different aperture sizes are also presented and compared to previous spanwise correlation measurements made using multi-beam Malley Probes [3], CFD simulation [6], and other available 2-D wavefront measurements [11]. The spanwise correlation function was also found to be a function of the aperture size. While spanwise correlation functions based on 2-D wavefront data generally agree well with each other, the Malley-Probe-based spanwise correlation lengths were found to be consistently smaller compared with the relevant 2-D wavefront results. The exact reason of the observed discrepancy is a topic of future investigation.

Acknowledgments

This work is supported by the Air Force Office of Scientific Research, Grant number FA9550-09-1-0449. The U.S. Government is authorized to reproduce and distribute reprints for governmental purposes notwithstanding any copyright notation thereon.

References

[1] Jumper, E.J., and Fitzgerald, E.J., "Recent Advances in Aero-Optics," *Progress in Aerospace Sciences,* 37, 299-339.

[2] M. Wang, A.Mani and S. Gordeyev,"Physics and Computation of Aero-Optics", *Annual Review of Fluid Mechanics*, Vol. 44, pp. 299-321, 2012. 7

[3] Cress, J. (2010) *Optical Aberrations Cause by Coherent Structures in a Subsonic, Compressible, Turbulent Boundary Layer,* PhD thesis, University of Notre Dame.

[4] Gordeyev, S. and Jumper, E.J., "Fluid Dynamics and Aero-Optics of Turrets", *Progress in Aerospace Sciences*, **46**, (2010), pp. 388-400.

[5] Duffin, D.A., "Feed-Forward Adaptive-Optic Correction of Aero-Optical Aberrations Caused by a Two-Dimensional Heated Jet," *36th AIAA Plasmadynamics and Lasers Conference*, Toronto, Ontario, Canada, Jun 2005. AIAA-2005-4776

[6] Wang, K. and Wang, M., "Aero-optics of subsonic turbulent boundary layers," *Journal of Fluid Mechanics*, Vol. 696, pp. 122-151, 2012.

[7] Gordeyev, S., Duffin, D., and Jumper, E.J., "Aero-Optical Measurements Using Malley Probe and High-Bandwidth 2-D Wavefront Sensors," *International Conference on Advanced Optical Diagnostics in Fluids, Solids, and Combustion*, Tokyo, Japan (2004).

[8] Gordeyev, S., Hayden, T., and Jumper, E.J., "Aero-Optical and Flow Measurements Over a Flat-Windowed Turret," *AIAA Journal*, Vol. **45**, No. 2, pp. 347-357, (2007).

[9] Cress, J., Gordeyev, S., Post, M, and Jumper E.J., "Aero-Optical Measurements in a Turbulent, Subsonic Boundary Layer at Different Elevation Angles," *39th AIAA Plasmadynamics and Lasers Conference*, Seattle, WA, June 2008, AIAA-2008-4214.

[10] Cress, J., Gordeyev, S., and Jumper E.J., "Aero-Optical Measurements in a Heated, Subsonic, Turbulent Boundary Layer," *48th AIAA Aerospace Sciences Meeting Including the New Horizons Forum and Aerospace Exposition*, AIAA-2010-434*,* Orlando, FL, January 2010.

[11] , D.J., Gordeyev, S., and Jumper, E.J., "Revised scaling of optical distortions caused by compressible, subsonic turbulent boundary layers," *38th AIAA Plasmadynamics and Lasers Conference*, AIAA-2007-4009, Miami, FL, June 2007.

[12] Wyckham, C.M. and Smits, A.J., "Aero-optic distortion in transonic and hypersonic turbulent boundary layers," *AIAA Journal*, 47(9), 2158-2168, September 2009.

[13] Smith, A.E., Gordeyev, S., and Jumper, E.J., "Recent Measurements of Aero-Optical Effects Caused by Subsonic Boundary Layers," *Acquisition, Tracking, Pointing, and Laser Systems Technologies XXVI, Proceedings of SPIE*, Vol. 8395, June 2012, Paper 8395-11.

[14] Siegenthaler, J.P. (2008) *Guidelines for adaptive-optic correction based on aperture filtration*, PhD thesis, University of Notre Dame.

[15] S.Gordeyev, J. Cress and E. Jumper, " Far-Field Intensity Drop-Outs Caused by Turbulent Boundary Layers", DEPS, Beam Control Conference, 23-26 May, 20011, Orlando, FL. Paper 11-BC-050

[16] De Lucca, N., Gordeyev S., and Jumper, E.J., "The Airborne Aero-Optics Laboratory, Recent Data," *Acquisition, Tracking, Pointing, and Laser Systems Technologies XXVI, Proceedings of SPIE*, Vol. 8395, June, 2012, Paper 8395-7.

[17] De Lucca, N., Gordeyev, S., and Jumper, E.J., "The Study of Aero-Optical and Mechanical Jitter for Flat Window Turrets," *50th AIAA Aerospace Sciences Meeting*, Nashville, Tennessee, Jan 2012, AIAA Paper 2012-0623.